Supplementary Information (SI) for New Journal of Chemistry.
This journal is © The Royal Society of Chemistry and the Centre National de la Recherche Scientifique 2026

*Supporting Information*

# A dopant-free porphyrin as hole-transporting material enabling over 18% efficiency in perovskite solar cell

Yanjiao Li, Xiaohan Liu,Yujia Fan,Mengxue Ma and Wei Zhang*

Key Laboratory of Applied Surface and Colloid Chemistry, Ministry of Education, School of Chemistry and Chemical Engineering, Shaanxi Normal University, Xi'an 710119, Shaanxi, China.

*Corresponding author. E-mail address: zw@snnu.edu.cn

# Experimental

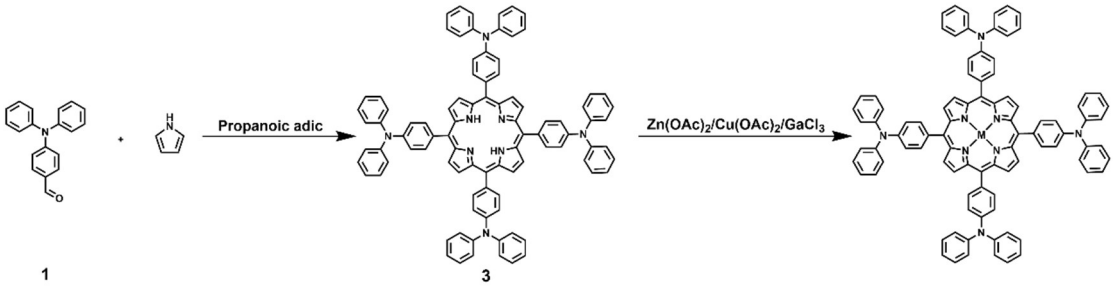


**Scheme S1.** The synthetic route for the porphyrin P-TPA

## Synthesis of P-TPA

A mixture of 4-(diphenylamino) benzaldehyde (2.73 g) in propionic acid (30 mL) was added with pyrrole (0.82 mL). The reaction mixture was heated to 130 °C and maintained under reflux for 3 h. After completion, the mixture was allowed to cool gradually to room temperature. The propionic acid was then removed by distillation, and the crude product was purified by column chromatography (*n*-hexane/ $CH_2Cl_2$) followed by recrystallization ($CH_2Cl_2$/$CH_3OH$) to afford the target compound in 8.03% yield.

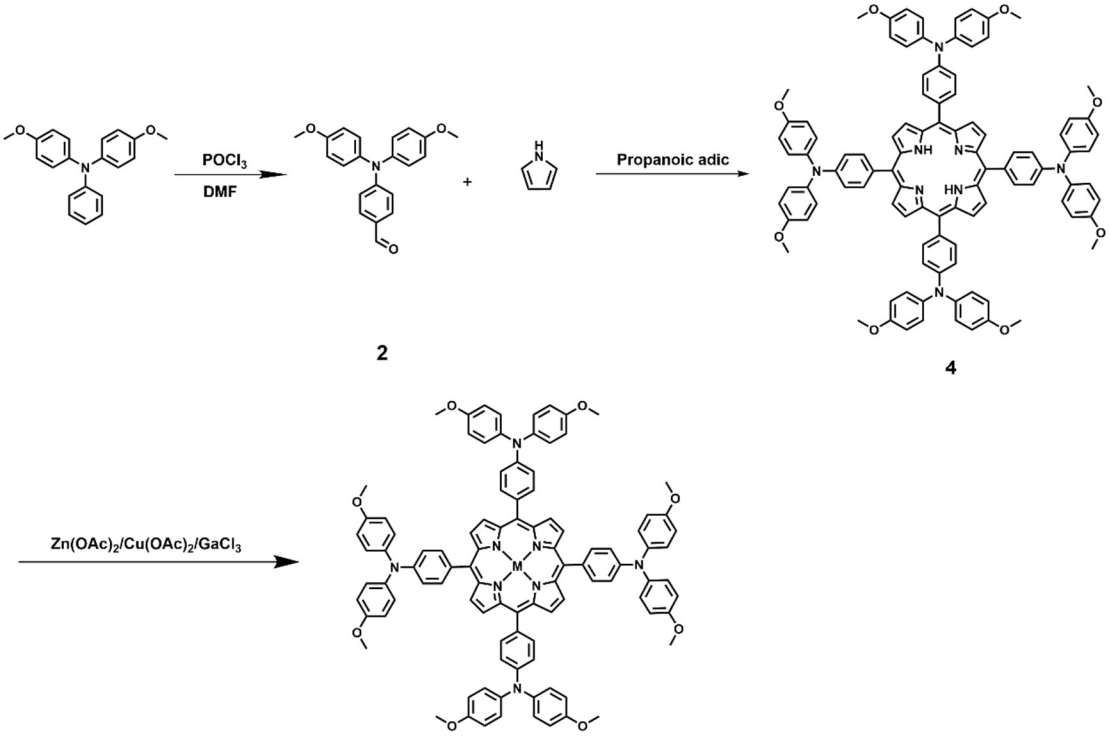


**Scheme S2.** The synthetic route for the porphyrin P-TPA-OMe

**Synthesis of P-TPA-OMe**

To the stirred solution of 4-methoxy-N-(4-methoxyphenyl)-N-phenylbenzen-amine (1.5 g) in dimethylformamide (30 mL), $POCl_3$ (1.17mL) was added dropwise at 0 °C under $N_2$. The reaction was performed at 90 °C under stirring for 3 h. After rotary evaporation of the solvent, the residue was dissolved in $CHCl_3$ and washed with a saturated $CH_3COONa$ aqueous solution. The organic layer was dried over $Na_2SO_4$. After removal of the solvent, the crude product was purified on the silica gel column ($CH_2Cl_2$/*n*-hexane = 1/1) to afford the target compound (1.4 g, 85.89% yield). 4-[Bis (4-methoxyphenyl) amino]-benzaldehyde (2 g) was dissolved in propionic acid (20 mL). Pyrrole (0.49 mL) was added, and the reaction mixture was heated to 130 °C under reflux for 3 h. Upon completion, the mixture was gradually cooled to room temperature. The propionic acid was removed by distillation, and the crude product was purified by column chromatography (*n*-hexane/$CH_2Cl_2$) followed by recrystallization ($CH_2Cl_2$/$CH_3OH$) to afford the ligand P-TPA-OMe in 6.56% yield.

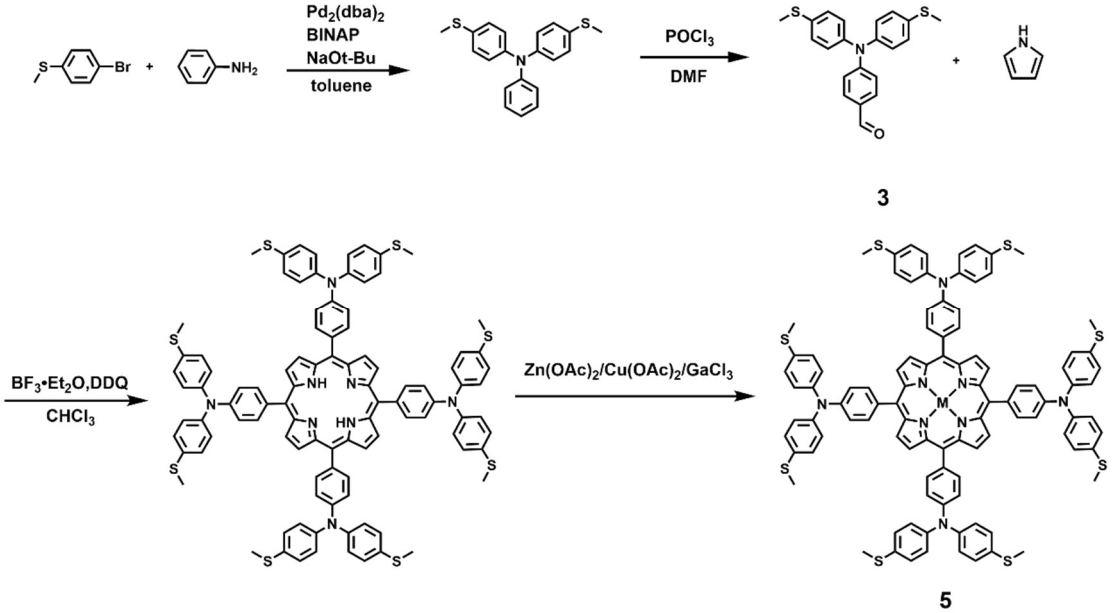


**Scheme S3**. The synthetic route for the porphyrin P-TPA-SMe

**Synthesis of P-TPA-SMe**

The ligand P-TPA-SMe was synthesized via a multi-step procedure. First, a one-pot reaction of 4-bromothioanisole with aniline, catalyzed by $Pd_2(dba)_3$/BINAP, yielded the key intermediate, 4-((methylthio)phenyl)-N-(4-(methylthio)phenyl)aniline. Subsequently, this intermediate was formylated using a Vilsmeier-Haack reaction ($POCl_3$/DMF) to give 4-(bis(4-(methylthio)phenyl)amino)-benzaldehyde. Finally, this aldehyde was condensed with pyrrole under $BF_3 \cdot Et_2O$ catalysis, followed by DDQ oxidation, to afford the target porphyrin ligand P-TPA-SMe in 7.09% overall yield for the final step.

**Synthesis of $P_{Zn}$-TPA/$P_{Zn}$-TPA-OMe/$P_{Zn}$-TPA-SMe**

The three ligands, P-TPA, P-TPA-OMe, and P-TPA-SMe, were separately dissolved in chloroform. Zinc acetate ($Zn(OAc)_2$) was weighed in a 1:10 molar ratio (ligand-to-metal), dissolved in a minimal amount of methanol, and added to the flask containing the ligand solution. The reaction mixture was heated to 70 °C and stirred under reflux for 4 hours. After completion, the mixture was cooled to room temperature. The organic phase was extracted, concentrated under reduced pressure to remove the solvent, and purified by recrystallization ($CH_2Cl_2$/*n*-hexane) to afford the final metalloporphyrin products (83 mg) with yields of 85.09%, 80.10%, and 79.03%, respectively.

**$P_{Zn}$-TPA:**

$^1$H NMR ($CDCl_3$, 400MHz, ppm): δ9.12 (s,8H), δ8.10 (d, J=8.0Hz, 8H), δ7.48 (m, 40H), δ7.17 (m, 8H) MALDI-TOF-MS: m/z: calcd. for C92H64N8Zn: 1346.96; found 1346.45.

**$P_{Zn}$-TPA-OMe**

$^1$H NMR ($CDCl_3$, 400MHz, ppm): δ9.09 (s,8H), δ8.16 (d, J=12.0Hz, 8H), δ7.29 (d, J=12.00Hz, 16H), δ6.99 (d, J=8.0Hz, 16H). δ3.86 (s, 24H). MALDI-TOF-MS: m/z: calcd. for C92H110N6O8Zn 1587.17; found 1586.5.

**$P_{Zn}$-TPA-SMe**

$^1$H NMR ($CDCl_3$, 400MHz, ppm): δ9.09 (s,8H), δ8.10 (d, J=12.0Hz, 8H), δ7.45 (d, J=8.00Hz, 8H), δ7.34 (m, 32H) δ2.50(s,24H). MALDI-TOF-MS: m/z: calcd. for C100H80N8S8Zn: 1715.66; found 1714.35.

**Synthesis of $P_{Cu}$-TPA/$P_{Cu}$-TPA-OMe/$P_{Cu}$-TPA-SMe**

The synthesis was performed analogously to the zinc complex.

$P_{Cu}$-TPA: MALDI-TOF-MS: m/z: calcd. for C92H64N8Cu: 1346.96; found 1345.13.

$P_{Cu}$-TPA-OMe: MALDI-TOF-MS: m/z: calcd. for C100H80N8O8Cu: 1585.33; found1584.6.

$P_{Cu}$-TPA-SMe: MALDI-TOF-MS: m/z: calcd. for C100H80N8S8Cu: 1713.82; found1713.35.

**Synthesis of $P_{Ga}$-TPA/$P_{Ga}$-TPA-OMe/$P_{Ga}$-TPA-SMe**

The metallation reactions were conducted in a nitrogen-filled glovebox. Each porphyrin ligand (P-TPA, P-TPA-OMe, or P-TPA-SMe) was separately dissolved in anhydrous DMF. Gallium trichloride ($GaCl_3$) was then added to the ligand solution in a schlenk flask at a ligand-to-metal molar ratio of 1:10. The reaction mixture was heated to 100 °C and stirred under reflux for 24 h. After the reaction was complete, the system was allowed to cool naturally to room temperature. The crude product was extracted, and the organic phase was concentrated by rotary evaporation to remove the solvent. Further

purification was carried out by recrystallization from a dichloromethane/*n*-hexane solvent system. The final gallium-porphyrin complexes were obtained with yields of 67.03%, 52.10%, and 50.03% for the P-TPA, P-TPA-OMe, and P-TPA-SMe derivatives, respectively.

$P_{Ga}$-TPA:

$^1$H NMR ($CDCl_3$, 400MHz, ppm): δ9.25 (s,8H), δ8.07 (d, 8H), δ7.48 (m, 40H), δ7.18 (m, 8H) MALDI-TOF-MS: m/z: calcd. for C92H64N8ClGa: 1386.75; found 1386.42.

$P_{Ga}$-TPA-OMe:

$^1$H NMR ($CDCl_3$, 400MHz, ppm): δ9.21 (s,8H), δ8.00 (d, 8H), δ7.39 (d, 16H), δ7.30 (d, 8H) MALDI-TOF-MS: m/z: calcd. for C100H80N8O8ClGa: 1626.96; found 1625.30.

$P_{Ga}$-TPA-SMe:

$^1$H NMR ($CDCl_3$, 400MHz, ppm): δ9.20 (s,8H), δ8.02 (d, 8H), δ7.45 (d, 8H), δ7.34 (m, 32H) MALDI-TOF-MS: m/z: calcd. for C100H80N8S8ClGa: 1755.45; found 1754.32.

## Device Fabrication and Characterization

The fluorine-doped tin oxide (FTO) substrates were initially etched using zinc powder in a 2 M hydrochloric acid solution, followed by sequential ultrasonic cleaning in deionized water, ethanol, and isopropanol (15 min each). Prior to film deposition, the cleaned substrates underwent a 10-min oxygen plasma treatment to enhance surface wettability. A $SnO_2$ electron transport layer was deposited onto the FTO substrates via chemical bath deposition at 90 °C. The double-cation perovskite film ($FA_{0.95}Cs_{0.05}PbI_3$) was fabricated using a one-step anti-solvent method. The perovskite precursor solution

(1.6 M) was prepared by dissolving FAI, CsI, and $PbI_2$ in a molar ratio of 0.95:0.05:1.05 in a mixed solvent of DMF and DMSO (4:1 v/v), with continuous stirring at room temperature for 6 h to ensure complete dissolution. The perovskite layer was deposited by spin-coating the precursor solution onto the substrate at 4000 rpm for 40 s (acceleration: 1000 rpm). At 25 s into the spin-coating process, 1000 μL of chlorobenzene (CB) was dripped onto the film as an anti-solvent. Subsequently, the substrates were transferred from the nitrogen-filled glovebox to ambient air (relative humidity < 40%) for thermal annealing at 150 °C for 15 min. After cooling to room temperature, the hole-transporting materials (HTMs) were deposited by spin-coating their chlorobenzene solutions at 3000 rpm for 30 s. The doped Spiro-OMeTAD solution (80 mg/mL in chlorobenzene) was prepared by adding 20 μL of Li-TFSI solution (520 mg/mL in acetonitrile) and 30 μL of 4-tert-butylpyridine (*t*BP) as dopants. Finally, a 200 nm-thick metal electrode was thermally evaporated onto the HTL to complete the device structure. For photovoltaic characterization, the fabricated perovskite solar cells (PSCs) were measured through a light-blocking aperture mask with an active area of 0.9 $cm^2$ to precisely define the illumination area.

## Device Analysis

Steady-state photoluminescence (PL, excitation wavelength: 532 nm) and time-resolved photoluminescence (TRPL) spectra were acquired using a Fluorolog-QM spectrofluorometer (Horiba, China). UV-vis absorption spectra were measured with a Lambda 1050 spectrophotometer (PerkinElmer, USA). Ultraviolet photoelectron spectroscopy (UPS) analysis was performed on an Escalab Xi+ spectrometer (Thermo

Fisher Scientific, USA) using monochromatic Al Kα radiation. $^{1}H$ nuclear magnetic resonance (NMR) spectra were recorded on a Bruker Ascend™ 400 MHz NMR spectrometer with tetramethylsilane (TMS) as an internal chemical shift reference. Electrochemical measurements were carried out with a CH Instruments 660E electrochemical workstation using a standard three-electrode configuration: a 3 mm diameter glassy carbon electrode as the working electrode, a platinum wire as the counter electrode, and an $Ag/AgNO_3$ electrode as the reference electrode. The supporting electrolyte was 0.1 M ($n\text{-}Bu_4NPF_6$) in dichloromethane solution. Cyclic voltammetry (CV) scans were performed at a scan rate of 50 mV/s, with all potentials calibrated against the $Fc/Fc^+$ redox couple as an internal standard. The photovoltaic performance of the devices was characterized by current density-voltage (J-V) measurements using a Sirius 2450 source meter coupled with an Enlitech IV-300A solar simulator under 100 $mW/cm^2$ illumination (AM 1.5G spectrum). The light intensity was calibrated prior to each measurement using an QE-B1 certified silicon reference cell. J-V curves were measured with both reverse (from 1.2 V to 0 V) and forward (from 0 V to 1.2 V) scans at a rate of 0.1 V/s. The active area of the devices was defined by a metal shadow mask to 0.09 $cm^2$. The surface morphology of the films was observed using a Hitachi SU8220 high-resolution field emission scanning electron microscope (SEM).

**Table S1.** Comparison of the photovoltaic performance between PGa-SMe and PCu-SMe in this work and recently reported high-performance HTMs.

| HTM | Device structure | Doped or not | Voc (V) | FF (%) | Jsc (mA/cm$^2$) | PCE (%) | Ref. |
|---|---|---|---|---|---|---|---|
| **$P_{Ga}$-SMe** | FTO/$SnO_2$/$FA_{0.95}Cs_{0.05}PbI_3$/HTM/Au | no | 1.10 | 63.72 | 26.28 | 18.40 | |
| **$P_{Cu}$-SMe** | FTO/$SnO_2$/$FA_{0.95}Cs_{0.05}PbI_3$/HTM/Au | no | 1.06 | 55.66 | 25.61 | 15.15 | |
| **Spiro-OMeTAD** | FTO/$SnO_2$/$FA_{0.95}Cs_{0.05}PbI_3$/HTM/Au | yes | 1.12 | 81.68 | 26.10 | 23.91 | |
| DCT | FTO/$SnO_2$/PVSK/HTM/$MoO_2$/Ag | no | 1.15 | 80.00 | 24.34 | 22.50 | [1] |
| DTTP-ThSO | ITO/$SnO_2$/PVSK/HEM/$MoO_2$/Ag | no | 1.14 | 81.30 | 24.73 | 22.81 | [2] |
| Cor-[DPA(2)]$_5$ | FTO/SnO2/PVSK/HTM/Au | no | 1.15 | 81.20 | 25.61 | 24.01 | [3] |
| CuLD | FTO/TiO2/PVSK/HTM/Au | no | 0.96 | 64.00 | 19.20 | 12.44 | [4] |
| MDA4 | FTO/$SnO_2$/$FA_{0.8}MA_{0.2}PbI_3$/Au | no | 1.13 | 81.30 | 24.56 | 22.67 | [5] |

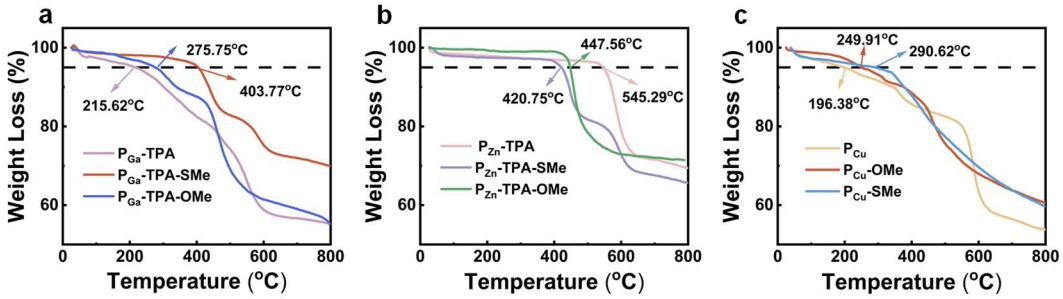


**Fig. S1** Thermogravimetric analysis of porphyrin HTMs measured with a heating rate of 10 °C $min^{-1}$.

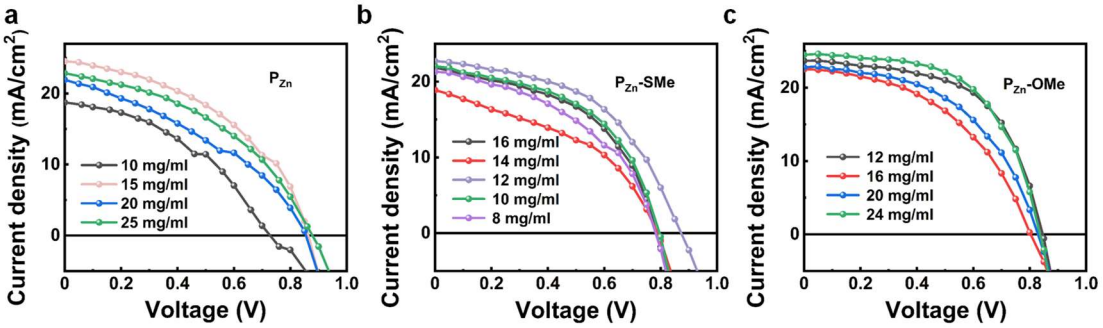


**Fig. S2** Current density-voltage (J-V) curves of the PSCs devices based on different concentrations of $P_{Zn}$ (a)、$P_{Zn}$-SMe (b)、$P_{Zn}$-OMe (c).

**Table S2**. J-V test parameters of $P_{Zn}$ hole transport material.

| $P_{Zn}$ | $V_{oc}$ (V) | $J_{sc}$ (mA cm$^{-2}$) | FF (%) | PCE (%) |
|---|---|---|---|---|
| 10 mg | 0.73 | 18.74 | 41.99 | 5.72 |
| 15 mg | 0.86 | 24.53 | 44.34 | 9.39 |
| 20 mg | 0.86 | 21.92 | 37.27 | 6.98 |
| 25 mg | 0.88 | 22.86 | 42.15 | 8.47 |

**Table S3.** J-V test parameters of $P_{Zn}$-SMe hole transport material.

| $P_{Zn}$-SMe | $V_{oc}$ (V) | $J_{sc}$ (mA cm$^{-2}$) | FF (%) | PCE (%) |
|---|---|---|---|---|
| 8 mg | 0.78 | 21.31 | 44.58 | 7.42 |
| 10 mg | 0.79 | 22.04 | 50.07 | 8.78 |
| 12 mg | 0.87 | 22.72 | 49.50 | 9.81 |
| 14 mg | 0.79 | 18.89 | 43.00 | 6.40 |

**Table S4.** J-V test parameters of $P_{Zn}$-OMe hole transport material.

| $P_{Zn}$-OMe | Voc (V) | Jsc (mA cm$^{-2}$) | FF (%) | PCE (%) |
|---|---|---|---|---|
| 12 mg | 0.85 | 23.68 | 57.89 | 11.60 |
| 16 mg | 0.83 | 22.54 | 46.56 | 8.43 |
| 20 mg | 0.83 | 22.79 | 50.58 | 9.56 |
| 24 mg | 0.84 | 24.49 | 57.95 | 11.87 |

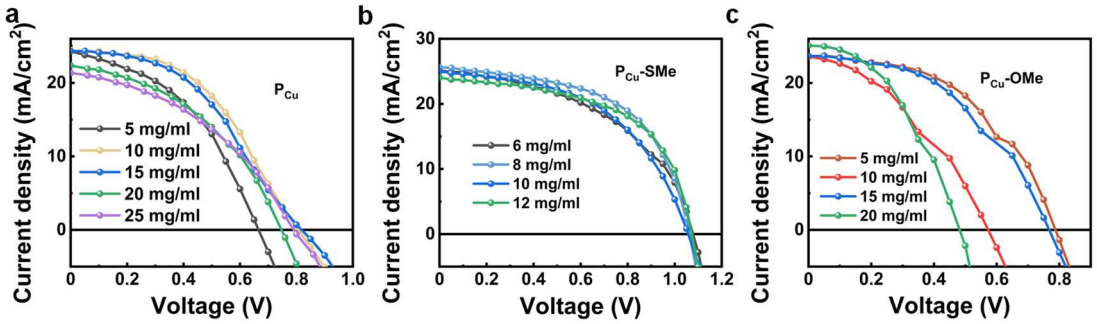


**Fig. S3** Current density-voltage (J-V) curves of the PSCs devices based on different concentrations of $P_{Cu}$ (a)、$P_{Cu}$-SMe (b)、$P_{Cu}$-OMe (c).

**Table S5.** J-V test parameters of $P_{Cu}$ hole transport material.

| $P_{Cu}$ | Voc (V) | Jsc (mA cm$^{-2}$) | FF (%) | PCE (%) |
|---|---|---|---|---|
| 5 mg | 0.66 | 24.32 | 42.97 | 6.96 |
| 10 mg | 0.80 | 24.44 | 46.20 | 9.11 |
| 15 mg | 0.82 | 24.31 | 43.29 | 8.61 |
| 20 mg | 0.75 | 22.36 | 42.36 | 7.09 |
| 25 mg | 0.79 | 21.37 | 40.60 | 6.87 |

**Table S6.** J-V test parameters of $P_{Cu}$-SMe hole transport material.

| $P_{Cu}$-SMe | Voc (V) | Jsc (mA cm$^{-2}$) | FF (%) | PCE (%) |
|---|---|---|---|---|
| 6 mg | 1.07 | 25.14 | 47.75 | 12.94 |
| 8 mg | 1.06 | 25.61 | 55.66 | 15.15 |
| 10 mg | 1.05 | 24.99 | 50.32 | 13.30 |
| 12 mg | 1.07 | 24.05 | 56.22 | 14.50 |
| 25 mg | 0.79 | 21.37 | 40.60 | 6.87 |

**Table S7.** J-V test parameters of $P_{Cu}$-OMe hole transport material.

| $P_{Cu}$-OMe | Voc (V) | Jsc (mA cm$^{-2}$) | FF (%) | PCE (%) |
|---|---|---|---|---|
| 5 mg | 0.78 | 23.54 | 49.20 | 9.12 |
| 10 mg | 0.57 | 23.57 | 37.05 | 5.00 |
| 15 mg | 0.76 | 23.66 | 46.21 | 8.39 |

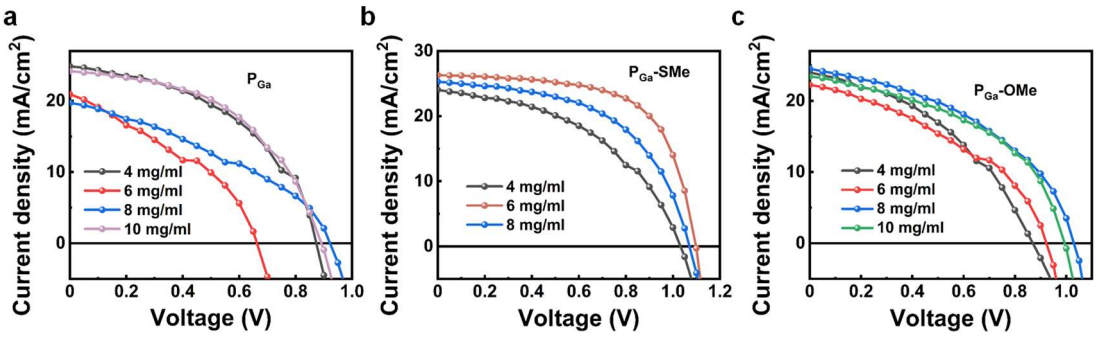


**Fig. S4** Current density-voltage (J-V) curves of the PSCs devices based on different concentrations of $P_{Ga}$ (a)、$P_{Ga}$-SMe (b)、$P_{Ga}$-OMe (c).

**Table S8.** J-V test parameters of $P_{Ga}$ hole transport material.

| $P_{Ga}$ | Voc (V) | Jsc (mA $cm^{-2}$) | FF (%) | PCE (%) |
|---|---|---|---|---|
| 4 mg | 0.87 | 24.85 | 47.17 | 10.24 |
| 6 mg | 0.66 | 20.92 | 37.62 | 5.22 |
| 8 mg | 0.92 | 19.71 | 36.92 | 6.71 |
| 10 mg | 0.89 | 24.17 | 49.29 | 10.62 |

**Table S9.** J-V test parameters of $P_{Ga}$-SMe hole transport material.

| $P_{Ga}$-SMe | Voc (V) | Jsc (mA $cm^{-2}$) | FF (%) | PCE (%) |
|---|---|---|---|---|
| 4 mg | 1.03 | 24.03 | 45.84 | 11.36 |
| 6 mg | 1.10 | 26.28 | 63.72 | 18.40 |
| 8 mg | 1.07 | 25.29 | 53.49 | 14.47 |
| 10 mg | 0.89 | 24.17 | 49.29 | 10.62 |

**Table S10.** J-V test parameters of $P_{Ga}$-OMe hole transport material.

| $P_{Ga}$-OMe | Voc (V) | Jsc (mA $cm^{-2}$) | FF (%) | PCE (%) |
|---|---|---|---|---|
| 4 mg | 0.87 | 24.01 | 41.04 | 8.57 |
| 6 mg | 0.92 | 22.24 | 39.81 | 8.17 |
| 8 mg | 1.02 | 24.53 | 43.89 | 11.08 |
| 10 mg | 0.99 | 23.42 | 46.70 | 10.86 |

**Table S11.** The J-V test parameters of PCu, PCu-SMe, and PCu-OMe hole transport materials at their optimal concentrations.

| | Voc (V) | Jsc (mA cm$^{-2}$) | FF (%) | PCE (%) |
|---|---|---|---|---|
| **$P_{Cu}$** | 0.80 | 24.44 | 46.20 | 9.11 |
| **$P_{Cu}$-SMe** | 1.06 | 25.61 | 55.66 | 15.15 |
| **$P_{Cu}$-OMe** | 0.78 | 23.54 | 49.20 | 9.12 |

**Table S12.**The J-V test parameters of PGa, PGa-SMe, and PGa-OMe hole transport materials at their optimal concentrations.

| | Voc (V) | Jsc (mA cm$^{-2}$) | FF (%) | PCE (%) |
|---|---|---|---|---|
| **$P_{Ga}$** | 0.89 | 24.17 | 49.29 | 10.62 |
| **$P_{Ga}$-SMe** | 1.10 | 26.28 | 63.72 | 18.40 |
| **$P_{Ga}$-OMe** | 1.03 | 24.53 | 43.89 | 11.08 |

**Table S13.**The J-V test parameters of PZn, PZn-SMe, and PZn-OMe hole transport materials at their optimal concentrations.

| | Voc (V) | Jsc (mA cm$^{-2}$) | FF (%) | PCE (%) |
|---|---|---|---|---|
| **$P_{Zn}$** | 0.86 | 24.53 | 44.34 | 9.39 |
| **$P_{Zn}$-SMe** | 0.87 | 22.72 | 49.49 | 9.81 |
| **$P_{Zn}$-OMe** | 0.84 | 23.68 | 57.89 | 11.60 |

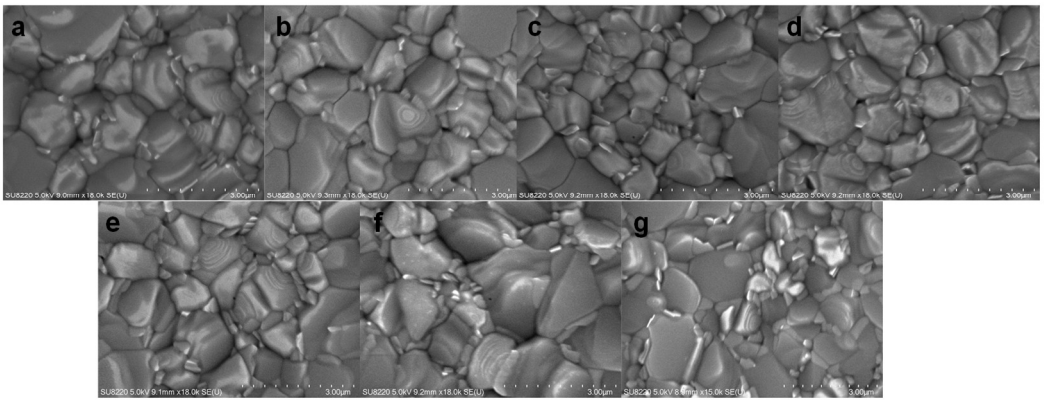


**Fig. S5** SEM images of (a) PVSK + $P_{Cu}$, (b) PVSK + $P_{Ga}$−SMe, and (c) PVSK + $P_{Zn}$−SMe. (d) PVSK + $P_{Ga}$-OMe, (e) PVSK + $P_{Cu}$-OMe, (f) PVSK + $P_{Zn}$-OMe, (g) PVSK + $P_{Zn}$.

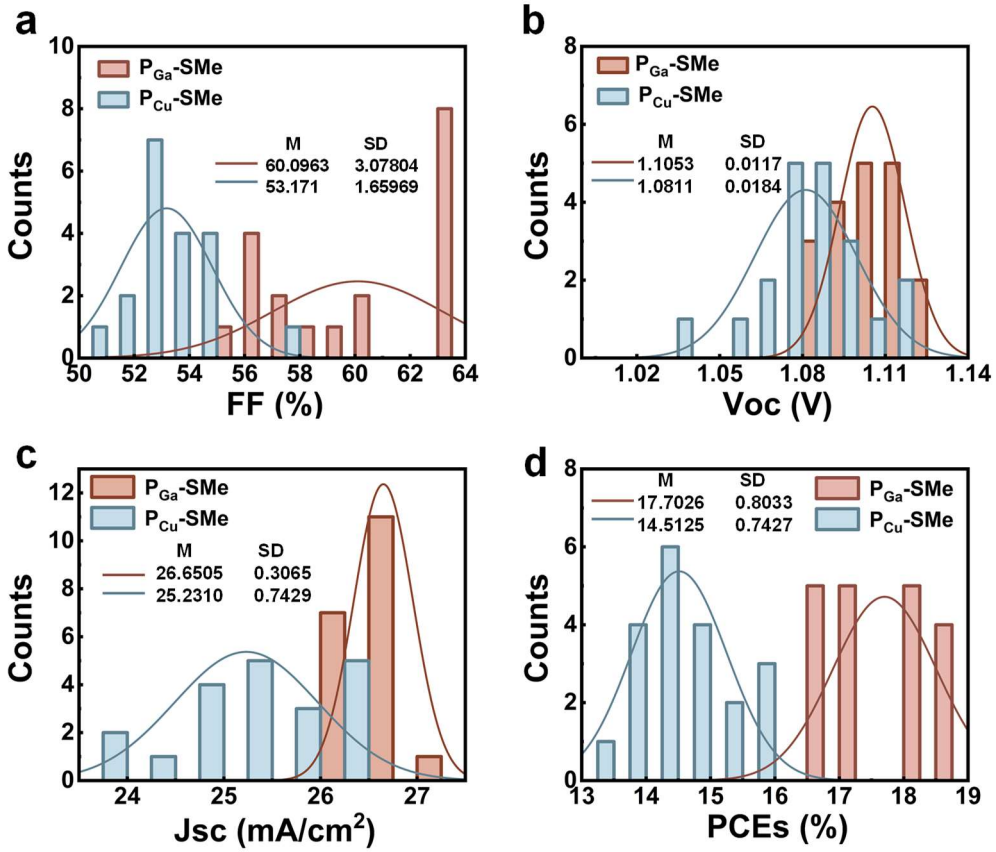


**Fig. S6** Histograms of (a) FF, (b) Voc, (c) Jsc, and (d) PCE for $P_{Ga}$-SMe and $P_{Cu}$-SMe.

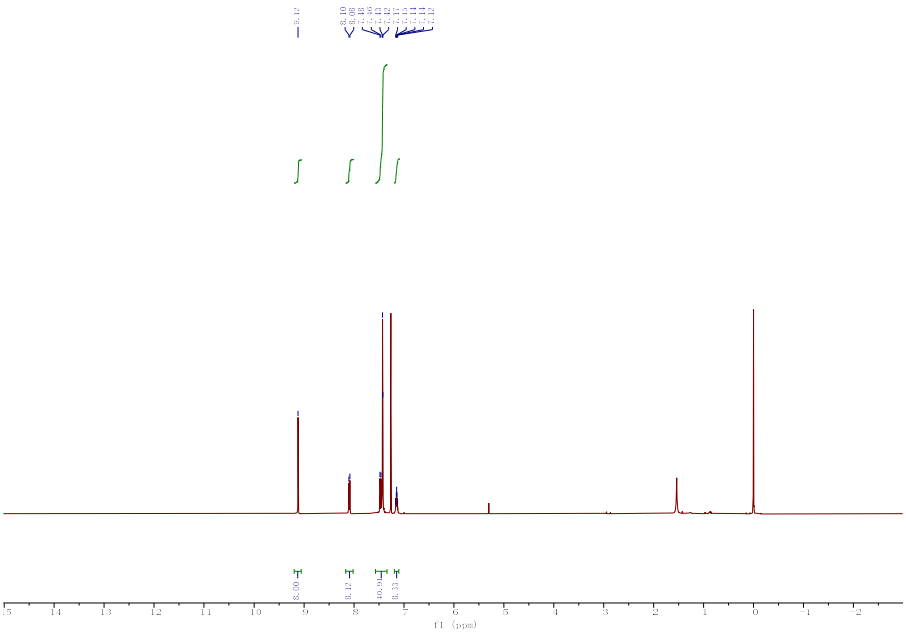

**Fig. S7** $^{1}$H-NMR of $P_{Zn}$-TPA in $CDCl_3$.

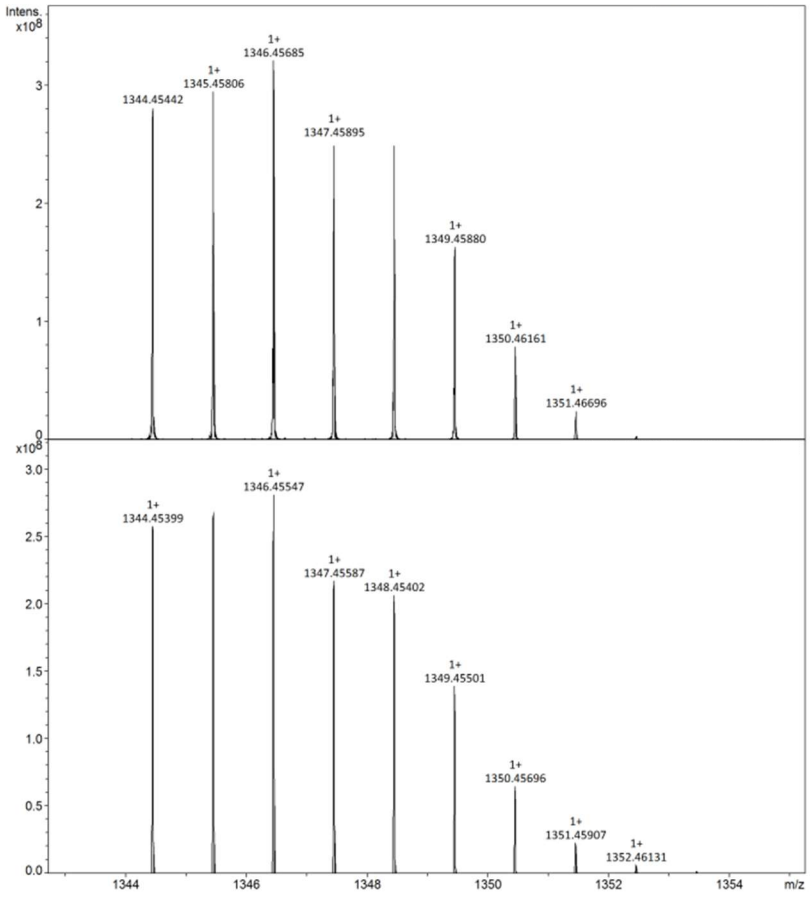


**Fig. S8** MALDI-TOF mass spectrum of $P_{Zn}$-TPA.

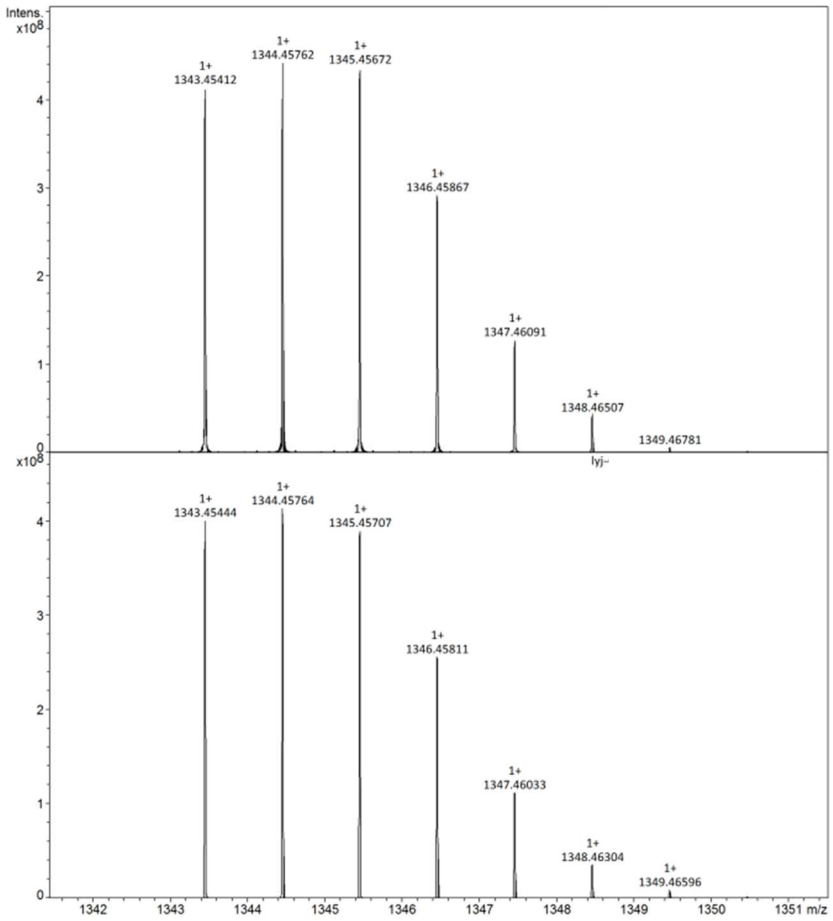


**Fig. S9** MALDI-TOF mass spectrum of $P_{Cu}$-TPA.

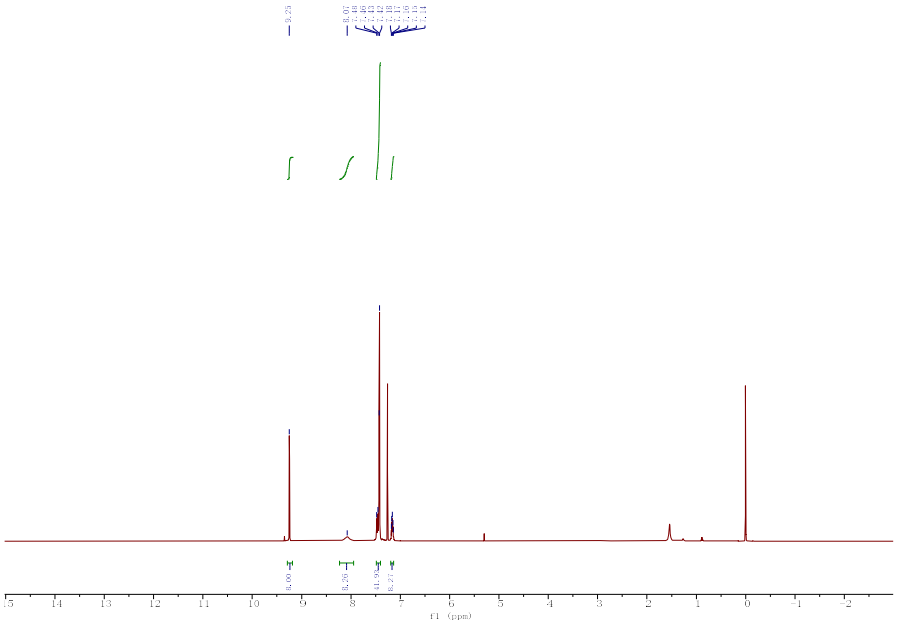


**Fig. S10** $^{1}$H-NMR of $P_{Ga}$-TPA in $CDCl_3$.

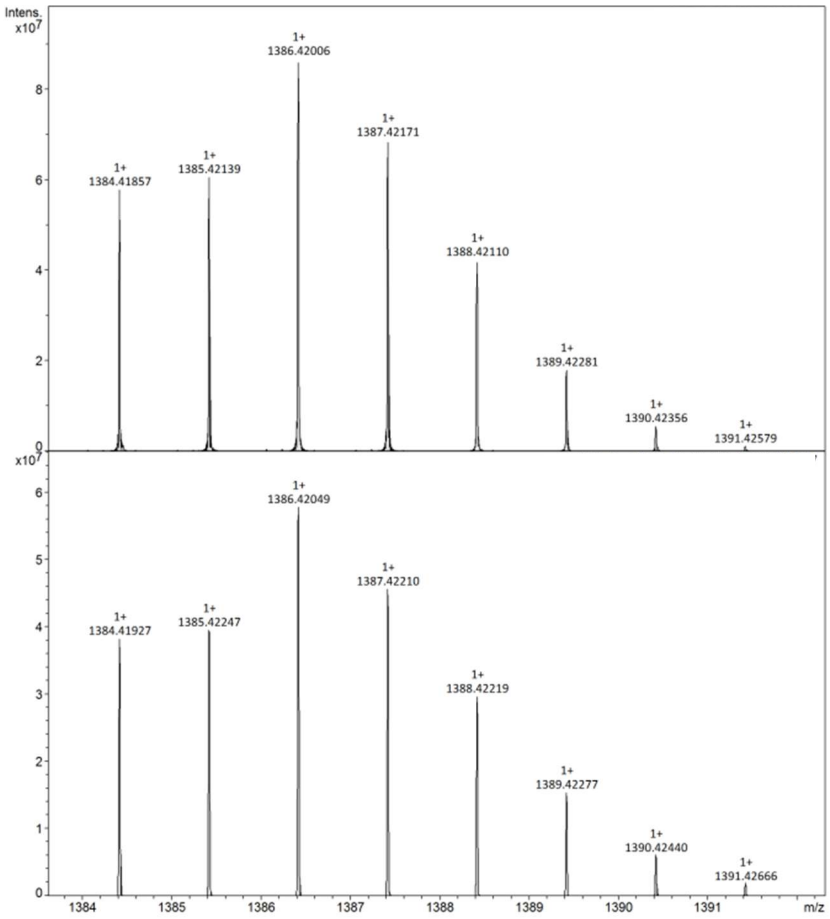


**Fig. S11** MALDI-TOF mass spectrum of $P_{Ga}$-TPA.

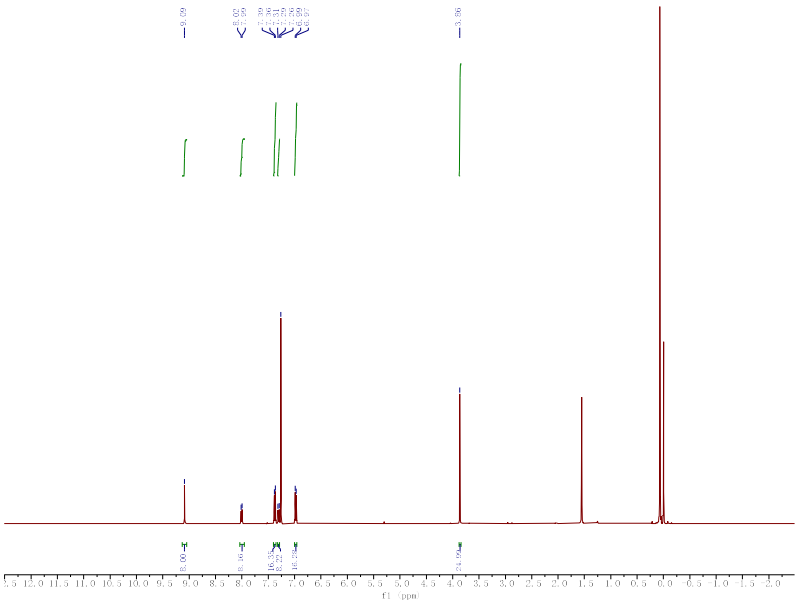

**Fig. S12** $^{1}$H-NMR of $P_{Zn}$-TPA-OMe in $CDCl_3$

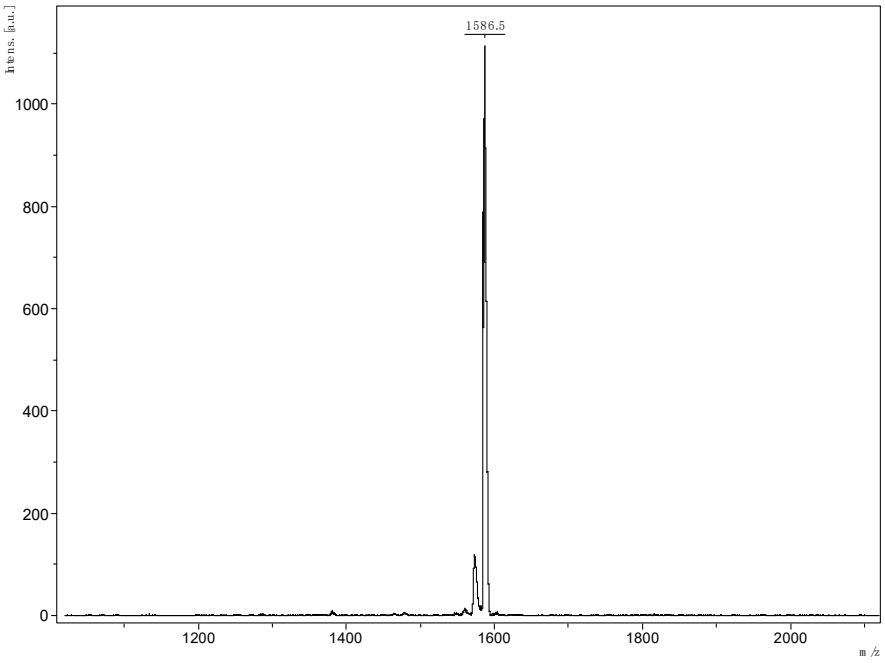


**Fig. S13** MALDI-TOF mass spectrum of $P_{Zn}$-TPA-OMe.

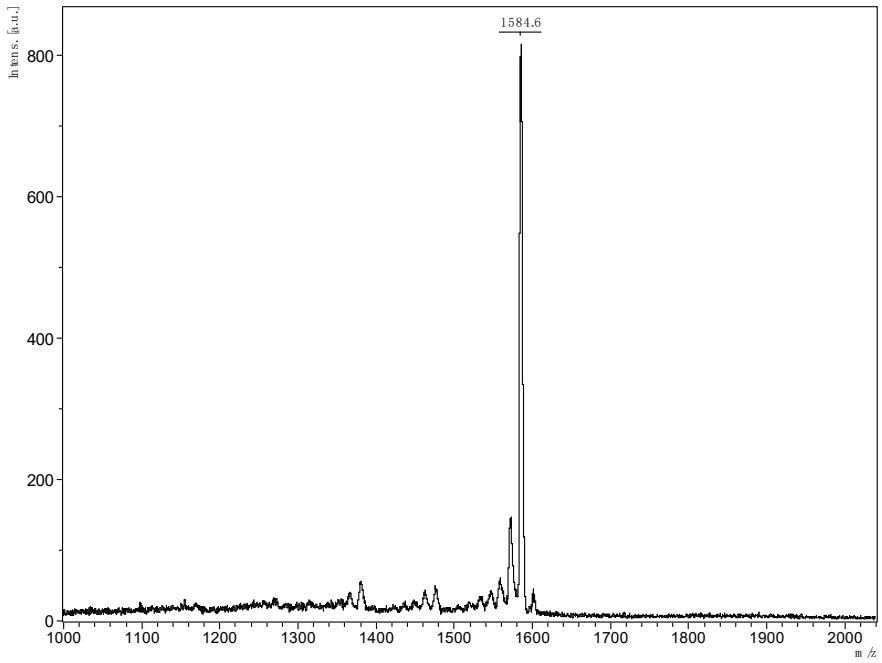


**Fig. S14** MALDI-TOF mass spectrum of $P_{Cu}$-TPA-OMe.

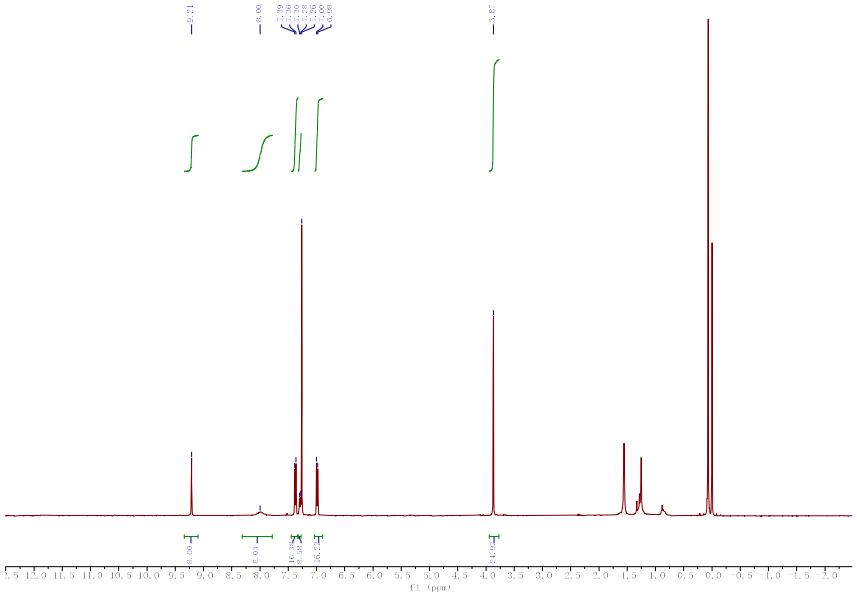

**Fig. S15** $^{1}$H-NMR of $P_{Ga}$-TPA-OMe in $CDCl_3$

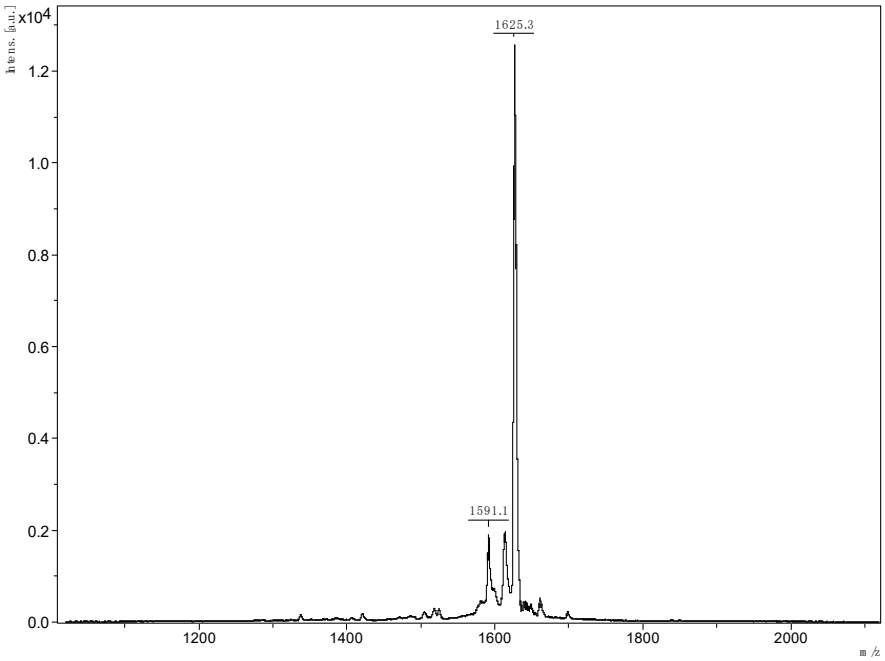


**Fig. S16** MALDI-TOF mass spectrum of $P_{Ga}$-TPA-OMe.

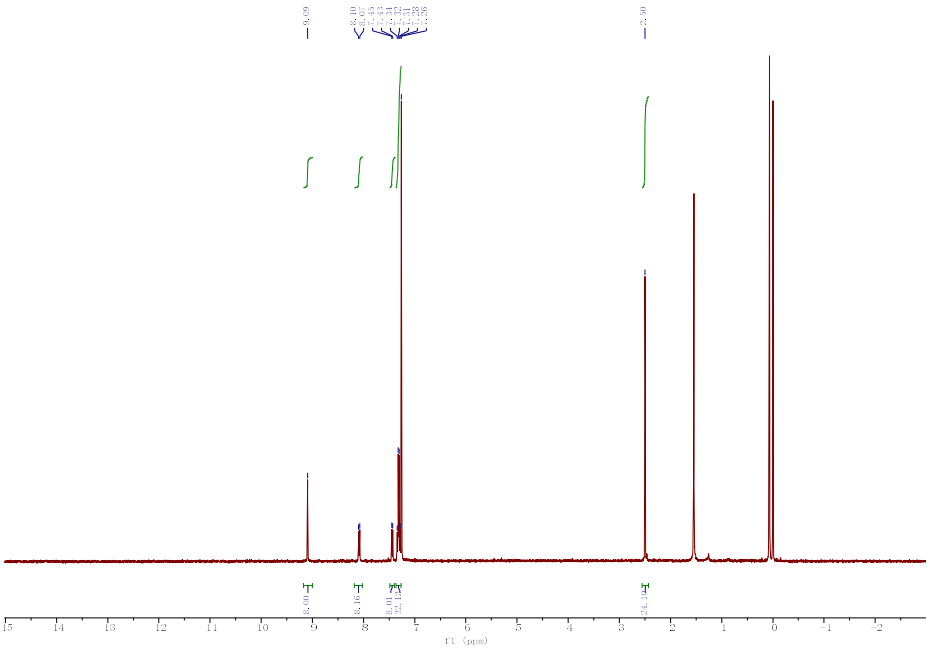

**Fig. S17** $^{1}$H-NMR of $P_{Zn}$-TPA-SMe in $CDCl_3$.

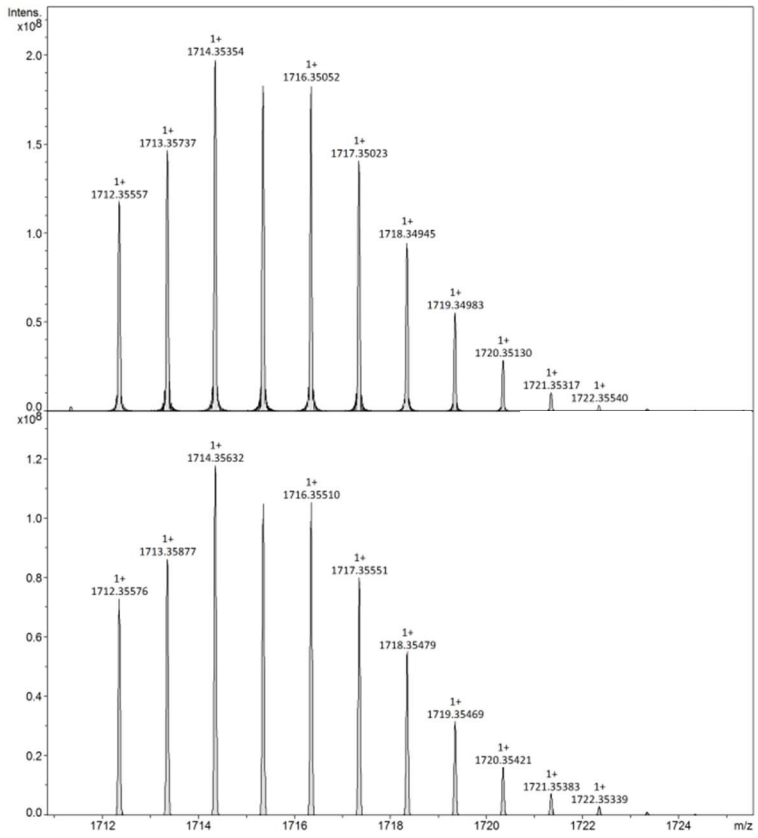


**Fig. S18** MALDI-TOF mass spectrum of $P_{Zn}$-TPA-SMe.

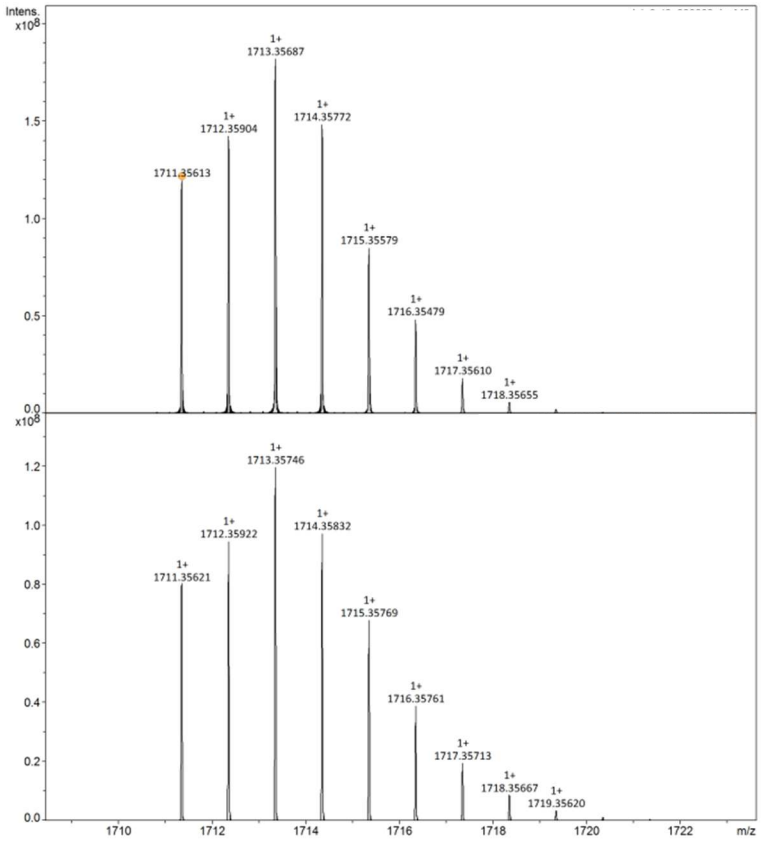


**Fig. S19** MALDI-TOF mass spectrum of $P_{Cu}$-TPA-SMe.

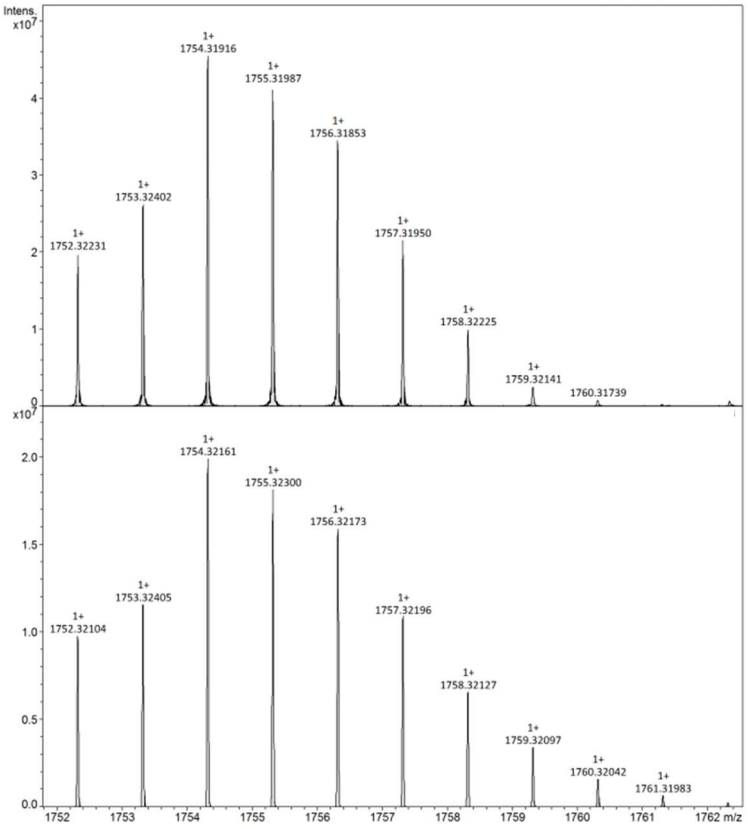


**Fig. S20** MALDI-TOF mass spectrum of $P_{Ga}$-TPA-SMe.


1 J. Tan, J. Zhang, H. Sun, K. Chen, X. Gao, P. Zhang, C. Zhong, F. Wu, Z. a. Li and L. Zhu, *Small*, 2024, **20**, 2407027.

2 G. Xie, J. Wang, S. Yin, A. Liang, W. Wang, Z. Chen, C. Feng, J. Yu, X. Liao, Y. Fu, Q. Xue, Y. Min, X. Lu and Y. Chen, *Angew. Chem. Int. Ed.*, 2024, **63**, e202403083.

3 X.-P. Zhang, L. Wang, W.-X. Zhang, Z.-C. Chen, C. Yang, S.-Y. Xu, P. Du, B.-W. Chen, Q. He, H.-R. Tian, X. Zhu, M. Li, S.-S. Wang, L.-L. Deng, S.-H. Chen, Q. Zhang, S.-Y. Xie and L.-S. Zheng, *Angew. Chem. Int. Ed.*, 2025, **64**, e202413582.

4 K. Devulapally, T. H. Chowdhury, Y. He, M. N. Rajesh, S. Prasanthkumar, A. Islam and L. Giribabu, *Journal of Photochemistry and Photobiology*, 2023, **16**, 100188.

5 C. L. Mai, Q. Xiong, X. Li, J. Y. Chen, J. Y. Chen, C. C. Chen, J. Xu, C. Liu, C. Y. Yeh and P. Gao, *Angew. Chem. Int. Ed.*, 2022, **61**. e202209365.